SCIENCE CHINA
Physics, Mechanics & Astronomy

• Article •
Editor's Focus

September 2022 Vol. 65 No. 9: 294262
https://doi.org/10.1007/s11433-022-1926-0

Editor's Focus

Spectrally multiplexed and bright entangled photon pairs in a lithium niobate microresonator

Bo-Yu Xu[1†], Li-Kun Chen[2†], Jin-Tian Lin[3†], Lan-Tian Feng[1,4†], Rui Niu[1,4], Zhi-Yuan Zhou[1,4], Ren-Hong Gao[3], Chun-Hua Dong[1,4], Guang-Can Guo[1,4], Qi-Huang Gong[2], Ya Cheng[3,5,6*], Yun-Feng Xiao[2,6*], and Xi-Feng Ren[1,4*]

[1] *CAS Key Laboratory of Quantum Information, University of Science and Technology of China, Hefei 230026, China;*
[2] *State Key Laboratory for Mesoscopic Physics and Frontiers Science Center for Nano-optoelectronics, School of Physics, Peking University, Beijing 100871, China;*
[3] *State Key Laboratory of High Field Laser Physics and CAS Center for Excellence in Ultra-intense Laser Science, Shanghai Institute of Optics and Fine Mechanics (SIOM), Chinese Academy of Sciences (CAS), Shanghai 201800, China;*
[4] *CAS Synergetic Innovation Center of Quantum Information & Quantum Physics, University of Science and Technology of China, Hefei 230026, China;*
[5] *State Key Laboratory of Precision Spectroscopy, East China Normal University, Shanghai 200062, China;*
[6] *Collaborative Innovation Center of Extreme Optics, Shanxi University, Taiyuan 030006, China*

Received May 5, 2022; accepted May 13, 2022; published online July 27, 2022

On-chip bright quantum sources with multiplexing ability are extremely high in demand for integrated quantum networks with unprecedented scalability and complexity. Here, we demonstrate a bright and broadband biphoton quantum source with spectral multiplexing generated in a lithium niobate microresonator system. Without introducing the conventional domain poling, the on-chip microdisk produces photon pairs covering a broad bandwidth promised by natural phase matching in spontaneous parametric down conversion. Experimentally, the multiplexed photon pairs are characterized by 30 nm bandwidth limited by the filtering system, providing over 40 multiplexing channels with a 0.8 nm channel spacing. Meanwhile, the generation rate reaches 5.13 MHz/μW with a coincidence-to-accidental ratio up to 804, and the quantum source manifests a high purity with a heralded single photon correlation $g_H^{(2)}(0) = 0.0098 \pm 0.0021$. Furthermore, the energy-time entanglement is demonstrated with an excellent interference visibility of 96.5% ± 2%. Such a quantum source at the telecommunication band paves the way for high-dimensional entanglement and future integrated quantum information systems.

quantum entangled source, spectral multiplexing, lithium niobate on insulator, microresonator

PACS number(s): 42.50.-p, 42.65.-k, 42.82.-m

Citation: B.-Y. Xu, L.-K. Chen, J.-T. Lin, L.-T. Feng, R. Niu, Z.-Y. Zhou, R.-H. Gao, C.-H. Dong, G.-C. Guo, Q.-H. Gong, Y. Cheng, Y.-F. Xiao, and X.-F. Ren, Spectrally multiplexed and bright entangled photon pairs in a lithium niobate microresonator, Sci. China-Phys. Mech. Astron. **65**, 294262 (2022), https://doi.org/10.1007/s11433-022-1926-0

*Corresponding authors (Ya Cheng, email: ya.cheng@siom.ac.cn; Yun-Feng Xiao, email: yfxiao@pku.edu.cn; Xi-Feng Ren, email: renxf@ustc.edu.cn)
†These authors contributed equally to this work.

1 Introduction

Integrated quantum photonics combining micron-scale fabrication techniques and quantum information carriers promises a new platform for quantum computation and communication systems [1-4]. For global quantum information processing, a systematic on-chip quantum device includes quantum sources [5, 6], quantum detectors [7, 8] and quantum transducers [9], etc. Among them, quantum sources lay the foundation for all integrated quantum networks [10], especially those capable of generating massive numbers of qubits [11]. So far, this target has been realized by raising the number of entangled photons or their dimensionality [12-16], technically fulfilled with an array of quantum sources [17] or post selection of multiple photon pairs [18]. Nevertheless, photonic sources with multiplexing ability, which can overcome the possible incompatibility between different on-chip implementations, provide an alternative approach [19].

Parametric processes including spontaneous parametric down conversion (SPDC) and spontaneous four wave mixing [16, 20, 21] are normally used to generate integrated photonic sources [22]. These approaches require materials possessing $\chi^{(2)}$ or $\chi^{(3)}$ nonlinearity, for which lithium niobate (LN), aluminum gallium arsenide (AlGaAs), silicon nitride (SiN), silicon (Si), etc., are appropriate candidates. Among all potential materials, LN is highly qualified for its superior $\chi^{(2)}$ nonlinear property [23, 24], which not only guarantees the efficiency of the parametric conversion process but provides high modulation capacity under superconducting temperature with the Pockels effect [25, 26]. These merits make LN a promising platform for fully integrated quantum photonics chips [26-30]. Nevertheless, with the commercialization of lithium niobate on insulator (LNOI) wafer and the development of related micro-fabrication techniques [31-34], versatile quantum photon pair sources have been realized on LNOI systems with structures like periodically poled lithium niobate (PPLN) waveguides [35, 36], microring resonators [37] and microdisk resonators [38] in recent years. Among them, disk-shaped whispering gallery mode microresonators not only have the characteristics of simple fabrication processes and uncomplicated experimental systems, but also support abundant modes for multiplexing applications [39-44]. Such a spectrally multiplexed quantum source can be used to increase the quantum channel capacity for high-density quantum-key-distribution systems [45, 46] or to realize frequency-encoded high-dimensional quantum information processing [47, 48].

Here, we experimentally achieve photon pairs generated on a high-quality LN microdisk with high brightness and spectral multiplexing, and the verified bandwidth covers the full channels of a commercial dense wavelength division multiplexing (DWDM) from 1535 to 1565 nm. The broad phase-matching window is fulfilled by a concise and solid setup utilizing the natural birefringence of LN in an X-cut microdisk. With this technique, strong and broadband nonlinearity could be achieved even without periodic poling. In the system, the crystal axis lies in the plane of the microdisk, making the propagation constant of transverse electric (TE) modes nonuniform. Consequently, the parametric process involving TE modes possesses an oscillating phase mismatching quantity azimuthally, which promises a broad phase-matching window similar to the quasi phase-matching technique. Besides, the extraction efficiency is optimized with two distinct tapered fibers for the coupling of visible pump light at 775 nm and orthogonally polarized photon pairs around 1550 nm respectively. The aforementioned design ensures a superior pair generation rate (PGR) over 5.13 MHz/μW as well as excellent purity of the source with a coincidence-to-accidental ratio (CAR) up to 804 and a heralded single photon correlation (HSPC) $g_H^{(2)}(0) = 0.0098 \pm 0.0021$. Moreover, the photon pair source is verified for energy-time entanglement with an excellent interference visibility of 96.5% ± 2.0%. This versatile photon pair source, possessing both high PGR and wide bandwidth, paves the way for a broad spectrum quantum information process with the integrated photonic chip.

2 Experimental configuration

The experimental setup has been illustrated in Figure 1(a). The microdisk is fabricated on LNOI by photolithography-assisted chemo-mechanical etching [49, 50] and a freestanding LN microdisk with a diameter of 93 μm with a smooth sidewall and a wedge angle of approximately 35° is finally applied, as shown in the scanning electron microscopy (SEM) images of Figure 1(a). In the experiment, the visible pump light from a continuous wave laser is launched into the LN microdisk via a fiber tip. Meanwhile, the generated signal and idler lights are collected by another tapered fiber specially designed for coupling at the communication band with the clockwise and counter-clockwise collection ratio around 20:1, which is a great promotion of the previous work [38]. For the characterization of the coupling efficiency, the pumping efficiency is estimated by monitoring the power coupled out of the pumping fiber when injecting a visible light through the collection fiber. When the power of the injected 775 nm laser $P_1 = 1.41$ mW, the transmitted power in the collection fiber and the read-out power in the pumping fiber are recorded as $P_2 = 0.63$ mW and $P_3 = 2.831$ μW orderly. Successively, the pumping efficiency $\eta = P_3/(P_1 - P_2)$ is calculated as 0.363%. The averaged collection efficiency is

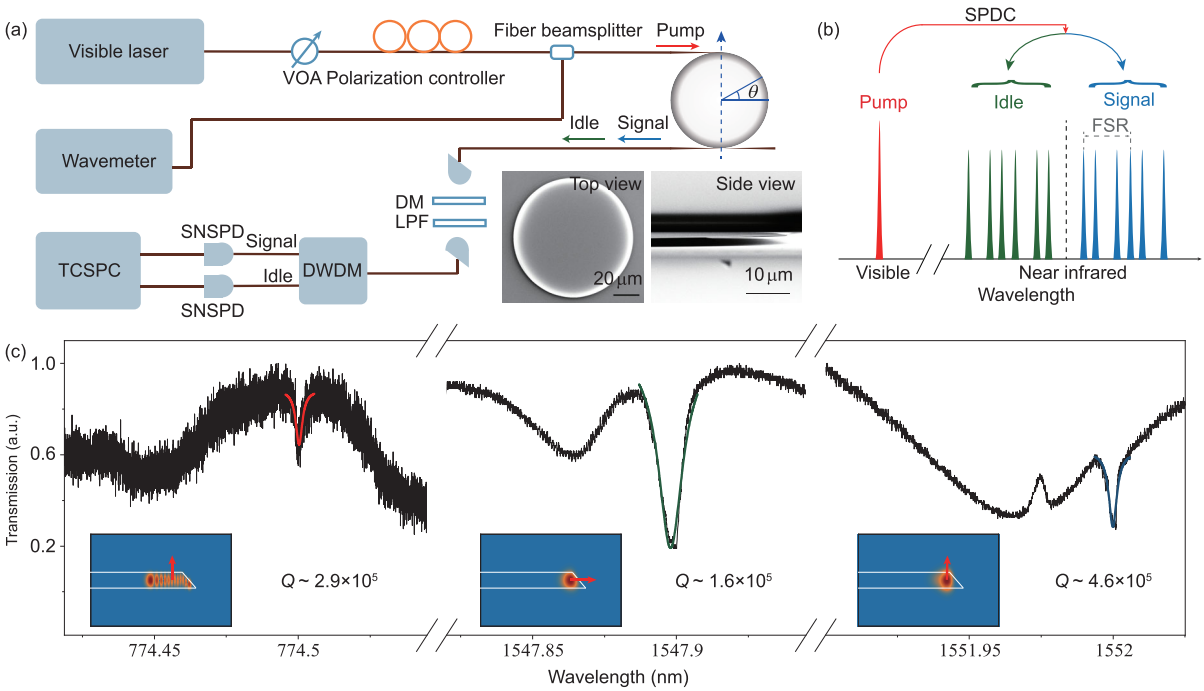

Figure 1 (Color online) (a) Experimental setup for quantum detection. The blue arrow in the microresonator denotes the crystal axis and θ is the azimuthal angle. Insets: SEM images of LN microdisk. (b) Schematic of generating broadband entangled photon pairs via non-degenerate SPDC. (c) Mode characterization at visible and near-infrared band. Insets: field distributions of corresponding modes, red arrows denote the polarization. VOA: variable optical attenuator; DM: dichroic mirror; LPF: 1400 nm long pass filter; SNSPD: superconducting nanowire single photon detectors; TCSPC: time-correlated single photon counting.

estimated by averaging the coupling efficiency for each resonant mode in the transmission spectrum when pumping an infrared light into the collection fiber. The collection efficiency for the modes at 1550 nm band is estimated as 55.6% for maximum and 25% on average, which is pulled down by the undercoupling of the modes with high radial mode numbers. In the case of the phase matching condition and energy conversation being fulfilled, the non-degenerate SPDC process will happen and a single pump photon will be converted into a signal photon and an idler photon. As illustrated in Figure 1(b), the broadband photon pairs are composed of two parts: one are the modes from different mode families within a free spectral range (FSR) and the other are the modes from the same mode family with an FSR interval. This feature distinguishes microdisk, which provides a multiplexed as well as narrow linewidth quantum source, from other devices like microrings or waveguides [36,37]. For the resonant modes characterization, the transmission spectra at 1550 and 780 nm are respectively acquired by pumping wavelength scanned lasers into the LN microdisk (Santec TSL-510 for 1500-1630 nm and New Focus TLB-6700 for 765-780 nm) through a tapered fiber. Obtained from transmission spectra, the FSR is estimated as 3.89 and 3.67 nm for the signal and idler light, respectively. In the meantime, the polarization of the light is tested through the scattering light parallel to the tapered fiber using a linear polarizer. It is proven that the non-degenerate SPDC photon pairs generate from a transverse magnetic (TM) mode at 774.86 nm with a high radial modal number to two corresponding orthogonally polarized modes with low radial modal numbers. The involved modes are then extracted and compared with the simulation results applying the experimental model in COMSOL Multiphysics, from which three characteristic modes are shown in Figure 1(c). With the existence of the non-uniform scattering loss at different wavelengths for the adhesion of the microdisk and fiber, the background lines of the transmission spectra are not as flat as the normalized level, which is widely observed [38,40]. Moreover, the loaded quality (Q) factor is 2.9×10^5 at the pump light wavelength and universally around 10^5 at signal and idler light wavelengths. It should be noted that the severe loss of Q factors from the intrinsic Q over 10^7 blames on the great scattering decline from the adhesion of the fiber and microdisk for the sake of system stability.

The signal is filtered by a dichroic mirror (DM) and a successive long pass filter (LPF) before entering the superconducting nanowire single photon detectors (SNSPD), ensuring the elimination of the pump light. Especially, the coincident counts spectrum is gathered through a DWDM with a 0.8 nm resolution and a 1535-1565 nm bandwidth. The spectrum is demonstrated at the signal light side of the photon pairs when the idler side is omitted for the symmetry of the spectrum, and the maximal coincident counts reach 350 in a 10 s

time integral with center wavelength at 1552.52 nm shown in Figure 2(a). The loss on the signal and idler light is estimated as 25 dB from the generation to detection. Precisely, the losses are calibrated as 2.2, 2.4, and 4 dB on the filtering opponents including the LPF, DM and DWDM. Moreover, the insertion and the transmission losses are respectively 8.7 and 3 dB. It should be noted that the shrinkage of coincident counts at longer wavelength results from the existence of material dispersion. At the longer wavelength, the detuning of the signal lights from the cavity resonance grows to exceed the linewidths of the modes. Limited by the range of the DWDM, the bandwidth of the generated photon pairs is within the range of 1535-1565 nm, which is supposed to be broader [38] with the calculation result in the next section.

3 Phase matching technique

Such a broadband photon pair generation is guaranteed by the natural phase-matching condition, which is assisted with the birefringence and the azimuthal modulation on the nonlinear effective index. The parametric process can be described in the quantum representation to analyze the signal intensity. To exhibit the mechanism of the broadband SPDC process in our regime, the interaction Hamiltonian between the pump light $\hat{E}_p$, signal light $\hat{E}_s$ and idler light $\hat{E}_i$ is introduced as [51,52]:

$$H_I(t) = \epsilon_0 \int_V \chi^{(2)}(\mathbf{r},t)\hat{E}_p^{(+)}(\mathbf{r},t)\hat{E}_s^{(-)}(\mathbf{r},t)\hat{E}_i^{(-)}(\mathbf{r},t)\mathrm{d}^3\mathbf{r} + H.c. \tag{1}$$

The continuous TM-polarized pump laser can be treated as the plane-wave in the form of

$$\hat{E}_p^{(+)}(\mathbf{r},t) = E_p \mathrm{e}^{-\mathrm{i}\mathbf{k}_p\cdot\mathbf{r}+\mathrm{i}\omega_p t}\hat{a}_p(\omega_p). \tag{2}$$

The orthogonally polarized versatile signal and idler lights can be treated as (q denotes the polarization):

$$\hat{E}_s^{(-)}(\mathbf{r},t) = \sum_{\mathbf{k}_s,q} E_{s,q}^* \mathrm{e}^{\mathrm{i}\mathbf{k}_s\cdot\mathbf{r}-\mathrm{i}\omega_s t}\hat{a}_{s,q}^\dagger(\omega_s), \tag{3}$$

$$\hat{E}_i^{(-)}(\mathbf{r},t) = \sum_{\mathbf{k}_i,q} E_{i,q}^* \mathrm{e}^{\mathrm{i}\mathbf{k}_i\cdot\mathbf{r}-\mathrm{i}\omega_i t}\hat{a}_{i,q}^\dagger(\omega_i), \tag{4}$$

where E_p, $E_{s,q}$ and $E_{i,q}$ are the quantized coefficients represented by $E_j = \mathrm{i}\sqrt{\hbar\omega_j/(4\pi\epsilon_0 c n_j)}$, $j = p, s, i$. $\hat{a}_p(\omega_p)$, $\hat{a}_{s,q}^\dagger(\omega_s)$ and $\hat{a}_{i,q}^\dagger(\omega_i)$ are the annihilation and creation operators of the pump, signal and idler lights, respectively. Moreover, in the weak signal approximation of the SPDC process, the state of the system can be represented by

$$|\Psi\rangle = |vac\rangle + \frac{1}{\mathrm{i}\hbar}\int_{-\infty}^{\infty} H_I(\tau)\,|vac\rangle\,\mathrm{d}\tau. \tag{5}$$

Then, substituting eq. (1) to eq. (5), the intensity of the signal can be obtained in the cylindrical coordinates under the conservation of energy.

$$P = \sum_{k_s,q}\sum_{k_i,q} A \iiint \hat{a}_p(\omega_p)\hat{a}_{s,q}^\dagger(\omega_s)\hat{a}_{i,q}^\dagger(\omega_i) \cdot \chi^{(2)}(\theta)\mathrm{e}^{\mathrm{i}(k_s+k_i-k_p)R\mathrm{d}\theta} r\mathrm{d}r\mathrm{d}\theta\mathrm{d}z. \tag{6}$$

It is clear that the generation intensity of the signal is composed of the overlap integral of electric fields intensity and the accumulation of phase difference. Specifically, the second order nonlinear coefficient $\chi^{(2)}$ can be subjected to an effective nonlinear coefficient with a fixed choice of the involved light polarization. In our system, it goes with $d_{\mathrm{eff}} = -d_{22}\cos\theta + d_{31}\sin\theta$ for two TM-polarized lights and one TE-polarized light participation. To elucidate the experimental results, a numerical simulation is employed in the Comsol Multiphysics with a model that has the same geometrical scale with the microdisk used in the experiment. Naturally, the refractive indice of TE-polarized light experiences an oscillation along the azimuthal angle due to the birefringence with $n_{\mathrm{TE}} = 1/\sqrt{\cos^2\theta/n_{\mathrm{o}}^2 + \sin^2\theta/n_{\mathrm{e}}^2}$, where n_{o} and n_{e} are the ordinary and extraordinary refractive indices of LN [40]. Thus, the phase mismatching quantity Δk oscillates in the same way. Meanwhile, the spatially modulated effective nonlinear coefficient d_{eff} can be written in the form of a Fourier

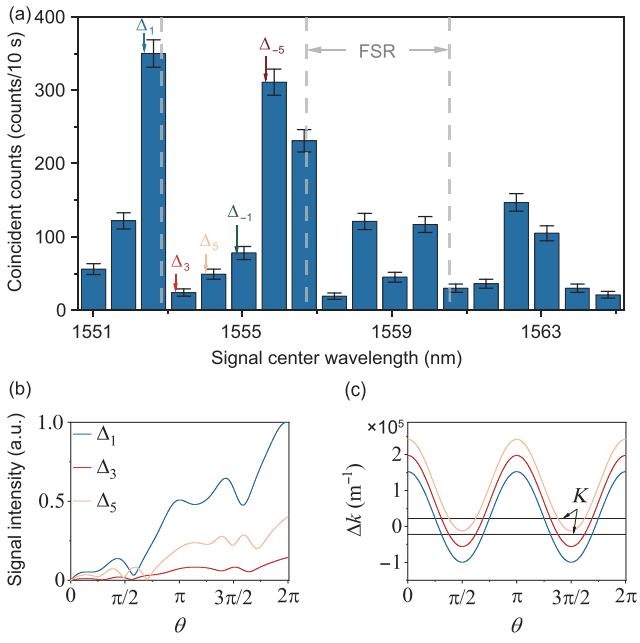

Figure 2 (Color online) (a) Spectrum of coincident counts presented by the signal light side at different channels of a DWDM with the pump power at 46.5 μW. The numbers denote different mode families with different phase-matching azimuthal modal number conditions Δm. (b) The growth of signal light intensity from different mode families along the azimuthal angle θ of the microresonator. (c) The oscillation of phase mismatching quantity Δk along θ.

expansion with first order series, which leads to a phase compensation term K. The concept of this natural phase matching condition is based on the quasi-phase matching technique, where the intersection points of the K and Δk stand for the reversal points of the total phase mismatching condition. This concept is primitively explored as cyclical phase-matching condition [53] and further improved in the theory. Considering the resonant condition of microdisk, the wave vector satisfies $n_{\text{eff}}kR = m$ where m is the azimuthal modal number. Namely, the phase mismatching quantity can be denoted as Δm, and it characterizes the phase-matching conditions of different mode families shown in Figure 2(a). The maximal coincident counts originated from two fundamental modes at the down conversion band as illustrated in Figure 1(c). In this case, the azimuthal and radial modal numbers (m, q) are (678, 12), (330, 1) and (349, 1) for the pump, signal and idler light separately. Besides, other phase-matched mode families for the signal and idler light have higher radial modal numbers, for example, (326, 2) and (347, 2) in the case of $\Delta m = -5$. The growth of the signal intensity P around a single loop integral is shown in Figure 2(b), and the intensity varies with different cases of Δm. It is obvious that the output signal intensity is dependent on the overlap of the modal fields as well as the phase mismatching quantity. Besides, the intersection between Δk and K promises a persistent accumulation of signal intensity beyond one loop. Such a requirement also restricts the choice of Δm in the range of $[-5, 5]$ partially shown in Figure 2(c). It should be noted that the resolution window of DWDM empirically contains multiple modes of the microdisk, thus the identification of mode families in Figure 2(a) is a bit rough. The phase matching window can be estimated by the comparison of the modal frequency mismatching $\Delta f = f_s + f_i - f_p$ and the modal linewidth (approximately 0.3 GHz) for the enhancement by double-resonance. As a simulation result, the resonant condition is fulfilled for the mode family Δ_1 at 1552-1647 nm band with the appearance of dispersion, resulting in a nearly 200 nm photon pair generation bandwidth in theory. Nevertheless, the dynamical tuning from the fiber-resonator coupling and the nonlinear process like thermal and photorefractive effect [54, 55] deviates the modes from the calculated eigenmodes, which narrows down the phase matching window in experiment.

4 Quantum characterization

To characterize the quantum source, we record the collective PGR and CAR free of DWDM filtering and the results are shown in Figure 3. Considering the lifetime of photons in the applied resonator is around 200 ps, the coincident window is set to be 0.8 ns to cover the coincident event. Typically, the PGR is calculated as PGR $= N_1N_2/N_{12}$, where N_1, N_2 and N_{12} are the counts for single detector and coincidence, respectively [56]. The power dependent curves of PGR and CAR are measured several times with different ranges of the input power. With the raise of the input power, the PGR tends to grow when the CAR falls, yielding a 1.81 MHz/μW PGR and up to 804 CAR. It is well acknowledged that this crossing relation of PGR and CAR results from the increase in multi-pair generation with the increase of input power. Moreover, the maximal efficiency of the SPDC is fitted as 5.13 MHz/μW in the narrow-range power tuning measurement.

Furthermore, we testify the single photon purity by measuring the HSPC function under a Hanbury Brown and Twiss experiment. The measurement is conducted under the condition that the corresponding DWDM channels possess the highest coincident counts with a collective PGR = 70.2 MHz. After the two-photon signal is input to the DWDM, the signal is output from two channels, one of which is directly connected to the TCSPC, and the other channel is split into two channels by a fiber BS and then connected to the TCSPC. The correlation function is gathered by $g_H^{(2)}(\tau) = N_{is_1s_2}N_i/N_{is_1}N_{is_2}$, where N_i is the counts of idler photons, N_{is_1}, N_{is_2} and $N_{is_1s_2}$ are the coincident counts between two-path and three-path, respectively. τ is the delay time of the electronic trigger pulses from one detector for signal photons with respect to the idler photons. For quantum on-chip opera-

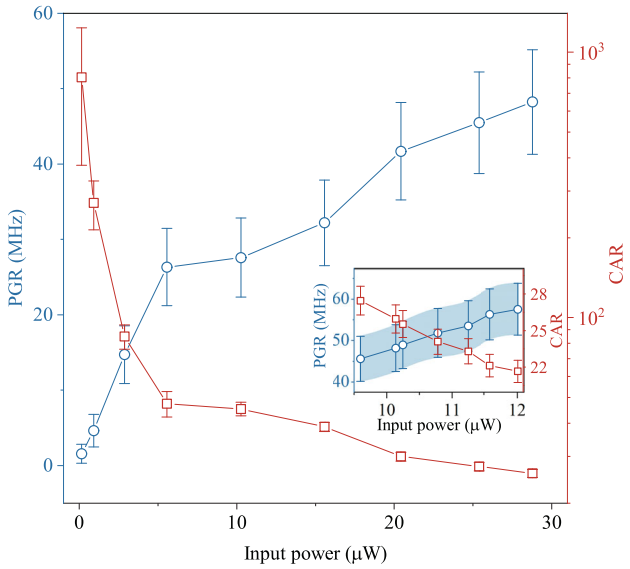

Figure 3 (Color online) Power dependence of PGR and CAR in a wide input power range measurement. Inset: maximal PGR reached in a narrow input power range measurement. The coincident counts are measured under the 85% efficiency of SNSPD and dark count rate below 100 Hz. The error bar is calculated by $\sqrt{N}$.

tions, we need to use photons from different channels, so we care more about the overall brightness of the quantum light source than the brightness of a certain channel, which is why we choose to calculate PGR in this way. As illustrated in Figure 4(a), the shape of $g_H^{(2)}$ forms an anti-bunching dip with an impressively low $g_H^{(2)}(0) = 0.0098 \pm 0.0021$, indicating an excellent single photon quality as an ultrabright quantum source.

Besides, the energy-time entanglement analysis is exhibited with the aid of a common unbalanced Michelson interferometer (UMI) with a 1.6 ns time difference. The measurement optical path is about the same as the experimental setup shown in Figure 1(a), the only difference is adding a UMI before the DWDM. The two-photon state is modulated in time, and three coincidence peaks are displayed in the TCSPC system with a time window of 0.8 ns. By post-selection of the central peak of the coincident counts with a proper time window, the state after post-selection is $|\Phi\rangle = \frac{1}{\sqrt{2}}(|SS\rangle + e^{2i\xi}|LL\rangle)$, where the first and second terms denote both signal and idler photons passing through the short (S) and long (L) arms of the UMI, and ξ is the phase difference introduced by UMI. The two-photon interference fringe is given in Figure 4(b), where a comparison between classical and quantum behaviors is also exhibited. Compared with classic coherent light from laser, it is clear that the interference period of classical light doubles that of quantum entangled light. Finally, the interference visibility is estimated as 96.5% ± 2.0% for the entangled state.

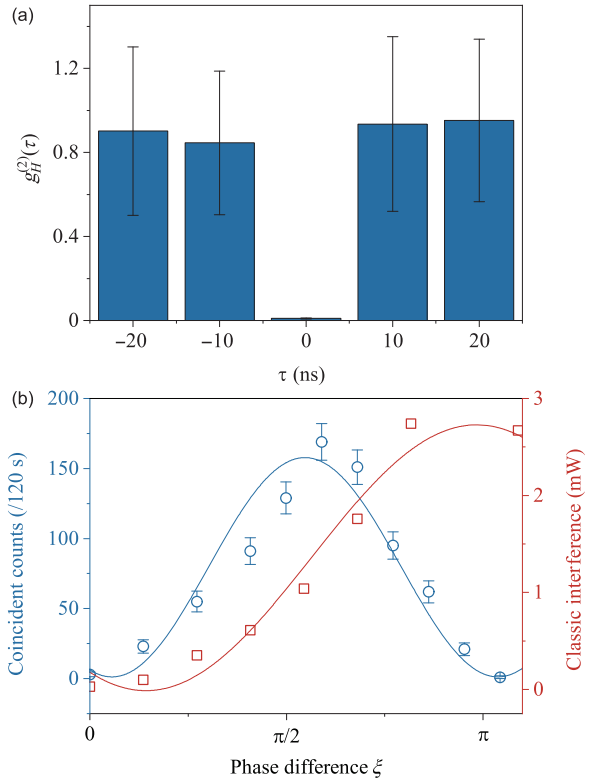

Figure 4 (Color online) (a) Single photon purity verification for HSPC function $g_H^{(2)}(\tau)$. Integral time: 1 h. (b) Two-photon energy-time entanglement measurement. Comparison between quantum and classical interference behaviors. Integral time: 120 s.

5 Summary

Disk-shaped microresonators naturally support abundant mode families, which is an appropriate platform to accomplish broadband source generation through natural phase-matching condition. Besides, the considerable quality factor of this microdisk ensures a concise and robust system to fulfill resonant condition with broad bandwidth as well as high efficiency. As a result, a remarkable PGR at 5.13 MHz/μW and a spectral bandwidth over 30 nm limited by the DWDM are experimentally demonstrated. This is an excellent candidate for multi-channel frequency-encoded quantum computation and quantum communication processes. To our knowledge, the experimental configuration we present is unique in achieving ultra-high brightness and considerably broad bandwidth simultaneously, and the bandwidth can be further broadened towards the theoretical value of 200 nm with the promotion of the filtering devices. Meanwhile, due to the group velocity mismatching between different materials, the coupling efficiency of fiber-resonator system for cross-band coupling can be further optimized. Future designs including chaos-assisted broadband coupling [57] and integrated waveguide coupling may resolve this obstacle. Moreover, a multi-photon source can be promisingly acquired by switching the pump laser from a continuous wave to a pulsed one [12]. In conclusion, the combination of the multiplexing application and great brightness, together with the breakthrough of the micron-scale footprint makes our entangled photon source set a bright future for the integration of quantum networks.

This work was supported by the National Key R&D Program of China (Grant Nos. 2016YFA0301302, and 2016YFA0301700), National Natural Science Foundation of China (Grant Nos. 11825402, 61590932, 11774333, 62061160487, 12004373, 11734009, and 11874375), Anhui Initiative in Quantum Information Technologies (Grant No. AHY130300), Strategic Priority Research Program of the Chinese Academy of Sciences (Grant No. XDB24030601), Beijing Academy of Quantum Information Sciences (Grant No. Y18G20), and Fundamental Research Funds for the Central Universities. This work was partially carried out at the USTC Center for Micro and Nanoscale Research and Fabrication. We thank W. Liu for helpful discussion.

1 J. Wang, F. Sciarrino, A. Laing, and M. G. Thompson, Nat. Photon. **14**, 273 (2020), arXiv: 2005.01948.
2 L. Feng, G. Guo, and X. Ren, Adv. Quantum Tech. **3**, 1900058 (2020).
3 J. W. Pan, Z. B. Chen, C. Y. Lu, H. Weinfurter, A. Zeilinger, and M. Żukowski, Rev. Mod. Phys. **84**, 777 (2012), arXiv: 0805.2853.

4 L. C. Kwek, L. Cao, W. Luo, Y. Wang, S. Sun, X. Wang, and A. Q. Liu, AAPPS Bull. **31**, 15 (2021).
5 X. Guo, C. L. Zou, C. Schuck, H. Jung, R. Cheng, and H. X. Tang, Light Sci. Appl. **6**, e16249 (2017), arXiv: 1603.03726.
6 T. J. Steiner, J. E. Castro, L. Chang, Q. Dang, W. Xie, J. Norman, J. E. Bowers, and G. Moody, PRX Quantum **2**, 010337 (2021).
7 J. P. Sprengers, A. Gaggero, D. Sahin, S. Jahanmirinejad, G. Frucci, F. Mattioli, R. Leoni, J. Beetz, M. Lermer, M. Kamp, S. Höfling, R. Sanjines, and A. Fiore, Appl. Phys. Lett. **99**, 181110 (2011), arXiv: 1108.5107.
8 S. Khasminskaya, F. Pyatkov, K. Słowik, S. Ferrari, O. Kahl, V. Kovalyuk, P. Rath, A. Vetter, F. Hennrich, M. M. Kappes, G. Gol'tsman, A. Korneev, C. Rockstuhl, R. Krupke, and W. H. P. Pernice, Nat. Photon. **10**, 727 (2016).
9 M. Mirhosseini, A. Sipahigil, M. Kalaee, and O. Painter, Nature **588**, 599 (2020).
10 D. Bunandar, A. Lentine, C. Lee, H. Cai, C. M. Long, N. Boynton, N. Martinez, C. DeRose, C. Chen, M. Grein, D. Trotter, A. Starbuck, A. Pomerene, S. Hamilton, F. N. C. Wong, R. Camacho, P. Davids, J. Urayama, and D. Englund, Phys. Rev. X **8**, 021009 (2018), arXiv: 1708.00434.
11 H. S. Zhong, H. Wang, Y. H. Deng, M. C. Chen, L. C. Peng, Y. H. Luo, J. Qin, D. Wu, X. Ding, Y. Hu, P. Hu, X. Y. Yang, W. J. Zhang, H. Li, Y. Li, X. Jiang, L. Gan, G. Yang, L. You, Z. Wang, L. Li, N. L. Liu, C. Y. Lu, and J. W. Pan, Science **370**, 1460 (2020), arXiv: 2012.01625.
12 M. Zhang, L. T. Feng, Z. Y. Zhou, Y. Chen, H. Wu, M. Li, S. M. Gao, G. P. Guo, G. C. Guo, D. X. Dai, and X. F. Ren, Light Sci. Appl. **8**, 41 (2019).
13 D. Llewellyn, Y. Ding, I. I. Faruque, S. Paesani, D. Bacco, R. Santagati, Y. J. Qian, Y. Li, Y. F. Xiao, M. Huber, M. Malik, G. F. Sinclair, X. Zhou, K. Rottwitt, J. L. O'Brien, J. G. Rarity, Q. Gong, L. K. Oxenlowe, J. Wang, and M. G. Thompson, Nat. Phys. **16**, 367 (2020).
14 L. T. Feng, M. Zhang, Z. Y. Zhou, M. Li, X. Xiong, L. Yu, B. S. Shi, G. P. Guo, D. X. Dai, X. F. Ren, and G. C. Guo, Nat. Commun. **7**, 11985 (2016), arXiv: 1601.06250.
15 J. Wang, S. Paesani, Y. Ding, R. Santagati, P. Skrzypczyk, A. Salavrakos, J. Tura, R. Augusiak, L. Mančinska, D. Bacco, D. Bonneau, J. W. Silverstone, Q. Gong, A. Acín, K. Rottwitt, L. K. Oxenlϕwe, J. L. O'Brien, A. Laing, and M. G. Thompson, Science **360**, 285 (2018), arXiv: 1803.04449.
16 L. T. Feng, M. Zhang, Z. Y. Zhou, Y. Chen, M. Li, D. X. Dai, H. L. Ren, G. P. Guo, G. C. Guo, M. Tame, and X. F. Ren, npj Quantum Inf. **5**, 90 (2019), arXiv: 1812.02368.
17 L. Li, Z. Liu, X. Ren, S. Wang, V. C. Su, M. K. Chen, C. H. Chu, H. Y. Kuo, B. Liu, W. Zang, G. Guo, L. Zhang, Z. Wang, S. Zhu, and D. P. Tsai, Science **368**, 1487 (2020).
18 X. W. Luo, X. Zhou, C. F. Li, J. S. Xu, G. C. Guo, and Z. W. Zhou, Nat. Commun. **6**, 7704 (2015), arXiv: 1512.08116.
19 M. Kues, C. Reimer, P. Roztocki, L. R. Cortés, S. Sciara, B. Wetzel, Y. Zhang, A. Cino, S. T. Chu, B. E. Little, D. J. Moss, L. Caspani, J. Azaña, and R. Morandotti, Nature **546**, 622 (2017).
20 X. Lu, Q. Li, D. A. Westly, G. Moille, A. Singh, V. Anant, and K. Srinivasan, Nat. Phys. **15**, 373 (2019), arXiv: 1805.04011.
21 P. Imany, J. A. Jaramillo-Villegas, O. D. Odele, K. Han, D. E. Leaird, J. M. Lukens, P. Lougovski, M. Qi, and A. M. Weiner, Opt. Express **26**, 1825 (2018).
22 A. Orieux, M. A. M. Versteegh, K. D. Jöns, and S. Ducci, Rep. Prog. Phys. **80**, 076001 (2017), arXiv: 1702.08823.
23 R. S. Weis, and T. K. Gaylord, Appl. Phys. A **37**, 191 (1985).
24 S. Saravi, T. Pertsch, and F. Setzpfandt, Adv. Opt. Mater. **9**, 2100789 (2021).
25 C. Wang, M. Zhang, X. Chen, M. Bertrand, A. Shams-Ansari, S. Chandrasekhar, P. Winzer, and M. Lončar, Nature **562**, 101 (2018).
26 R. Gao, J. Guan, N. Yao, L. Deng, J. Lin, M. Wang, L. Qiao, Z. Wang, Y. Liang, Y. Zhou, and Y. Cheng, Opt. Lett. **46**, 3131 (2021), arXiv: 2104.13501.
27 L. K. Chen, and Y. F. Xiao, Sci. China-Phys. Mech. Astron. **64**, 234264 (2021).
28 L. K. Chen, and Y. F. Xiao, Sci. China-Phys. Mech. Astron. **63**, 224231 (2020).
29 Q. Luo, Z. Z. Hao, C. Yang, R. Zhang, D. H. Zheng, S. G. Liu, H. D. Liu, F. Bo, Y. F. Kong, G. Q. Zhang, and J. J. Xu, Sci. China-Phys. Mech. Astron. **64**, 234263 (2021).
30 Y. A. Liu, X. S. Yan, J. W. Wu, B. Zhu, Y. P. Chen, and X. F. Chen, Sci. China-Phys. Mech. Astron. **64**, 234262 (2021), arXiv: 2009.12900.
31 C. Wang, M. J. Burek, Z. Lin, H. A. Atikian, V. Venkataraman, I. C. Huang, P. Stark, and M. Lončar, Opt. Express **22**, 30924 (2014), arXiv: 1410.2625.
32 J. Lin, Y. Xu, Z. Fang, M. Wang, J. Song, N. Wang, L. Qiao, W. Fang, and Y. Cheng, Sci. Rep. **5**, 8072 (2015).
33 M. Zhang, C. Wang, R. Cheng, A. Shams-Ansari, and M. Lončar, Optica **4**, 1536 (2017), arXiv: 1712.04479.
34 J. Lin, F. Bo, Y. Cheng, and J. Xu, Photon. Res. **8**, 1910 (2020).
35 G. T. Xue, Y. F. Niu, X. Liu, J. C. Duan, W. Chen, Y. Pan, K. Jia, X. Wang, H. Y. Liu, Y. Zhang, P. Xu, G. Zhao, X. Cai, Y. X. Gong, X. Hu, Z. Xie, and S. Zhu, Phys. Rev. Appl. **15**, 064059 (2021), arXiv: 2012.06092.
36 U. A. Javid, J. Ling, J. Staffa, M. Li, Y. He, and Q. Lin, Phys. Rev. Lett. **127**, 183601 (2021), arXiv: 2101.04877.
37 Z. Ma, J. Y. Chen, Z. Li, C. Tang, Y. M. Sua, H. Fan, and Y. P. Huang, Phys. Rev. Lett. **125**, 263602 (2020), arXiv: 2010.04242.
38 R. Luo, H. Jiang, S. Rogers, H. Liang, Y. He, and Q. Lin, Opt. Express **25**, 24531 (2017).
39 K. J. Vahala, Nature **424**, 839 (2003).
40 J. Lin, N. Yao, Z. Hao, J. Zhang, W. Mao, M. Wang, W. Chu, R. Wu, Z. Fang, L. Qiao, W. Fang, F. Bo, and Y. Cheng, Phys. Rev. Lett. **122**, 173903 (2019).
41 J. Lin, Y. Xu, J. Ni, M. Wang, Z. Fang, L. Qiao, W. Fang, and Y. Cheng, Phys. Rev. Appl. **6**, 014002 (2016).
42 J. Fürst, B. Sturman, K. Buse, and I. Breunig, Opt. Express **24**, 20143 (2016).
43 X. Ye, S. Liu, Y. Chen, Y. Zheng, and X. Chen, Opt. Lett. **45**, 523 (2020).
44 R. Xie, G. Li, F. Chen, and G. Long, Adv. Opt. Mater. **9**, 2100539 (2021).
45 Y. H. Li, Z. Y. Zhou, L. T. Feng, W. T. Fang, S. Liu, S. K. Liu, K. Wang, X. F. Ren, D. S. Ding, L. X. Xu, and B. S. Shi, Phys. Rev. Appl. **7**, 064005 (2017), arXiv: 1612.02915.
46 D. Aktas, B. Fedrici, F. Kaiser, T. Lunghi, L. Labonté, and S. Tanzilli, Laser Photon. Rev. **10**, 451 (2016), arXiv: 1601.02402.
47 C. Reimer, M. Kues, P. Roztocki, B. Wetzel, F. Grazioso, B. E. Little, S. T. Chu, T. Johnston, Y. Bromberg, L. Caspani, D. J. Moss, and R. Morandotti, Science **351**, 1176 (2016).
48 C. Reimer, S. Sciara, P. Roztocki, M. Islam, L. Romero Cortés, Y. Zhang, B. Fischer, S. Loranger, R. Kashyap, A. Cino, S. T. Chu, B. E. Little, D. J. Moss, L. Caspani, W. J. Munro, J. Azaña, M. Kues, and R. Morandotti, Nat. Phys. **15**, 148 (2019).
49 R. Wu, J. Zhang, N. Yao, W. Fang, L. Qiao, Z. Chai, J. Lin, and Y. Cheng, Opt. Lett. **43**, 4116 (2018), arXiv: 1806.00099.
50 M. Wang, R. Wu, J. Lin, J. Zhang, Z. Fang, Z. Chai, and Y. Cheng, Quantum Eng. **1**, e9 (2019).
51 Z. Yang, M. Liscidini, and J. E. Sipe, Phys. Rev. A **77**, 033808 (2008).
52 Y. X. Gong, Z. D. Xie, P. Xu, X. Q. Yu, P. Xue, and S. N. Zhu, Phys. Rev. A **84**, 053825 (2011), arXiv: 1112.4551.
53 G. Lin, J. U. Fürst, D. V. Strekalov, and N. Yu, Appl. Phys. Lett. **103**, 181107 (2013).
54 J. Wang, B. Zhu, Z. Hao, F. Bo, X. Wang, F. Gao, Y. Li, G. Zhang, and J. Xu, Opt. Express **24**, 21869 (2016).
55 X. Sun, H. Liang, R. Luo, W. C. Jiang, X. C. Zhang, and Q. Lin, Opt. Express **25**, 13504 (2017).
56 C. Xiong, G. D. Marshall, A. Peruzzo, M. Lobino, A. S. Clark, D. Y. Choi, S. J. Madden, C. M. Natarajan, M. G. Tanner, R. H. Hadfield, S. N. Dorenbos, T. Zijlstra, V. Zwiller, M. G. Thompson, J. G. Rarity, M. J. Steel, B. Luther-Davies, B. J. Eggleton, and J. L. O'Brien, Appl. Phys. Lett. **98**, 051101 (2011), arXiv: 1011.1688.
57 X. Jiang, L. Shao, S. X. Zhang, X. Yi, J. Wiersig, L. Wang, Q. Gong, M. Lončar, L. Yang, and Y. F. Xiao, Science **358**, 344 (2017).